Kirigami programming of monopole dynamics in artificial spin ice

Jinbo Yang,[1,2,3] Li Chen,[1,2,3] Qinlian Kang,[1,2,3] Guohonghao Zeng,[1,2,3] Ya Gao,[1,2,3] Yongfeng Mei,[1,2,3] Yizheng Wu,[2,4] and Jizhai Cui[1,2,3,*]

[1]*State Key Laboratory of Surface Physics & International Institute for Intelligent Nanorobots and Nanosystems, College of Intelligent Robotics and Advanced Manufacturing, Fudan University, Shanghai 200438, China*

[2]*Shanghai Key Laboratory of Metasurfaces for Light Manipulation, Fudan University, Shanghai 200433, China*

[3]*Zhejiang Key Laboratory of Extreme Environment Functional Materials, Yiwu Research Institute of Fudan University, Yiwu 322000, Zhejiang, China*

[4]*Department of Physics, Fudan University, Shanghai 200438, China*

(Received 30 July 2025; revised 1 March 2026; accepted 9 March 2026; published 30 March 2026)

Precise control of emergent magnetic monopoles in artificial spin ice is pivotal for topological spin-based circuitry. We model a square-ice lattice on a "rotating squares" kirigami scaffold, so a single mechanical rotation angle θ reprograms dipolar couplings. Monte Carlo simulations and analytic results show θ not only drives a specific type of Dirac string tension through zero, reverses bound monopole motion, but also slows down and collimates the collective motion of multiple monopoles along nearly straight strings. The cut-and-fold design is based on a geometric principle that is inherently scale- and material-independent, offering a versatile route to reconfigurable "magnetricity" devices; the specific magnetic functionality, however, is determined by the chosen material and dimensions.

DOI: 10.1103/q1vr-p9v4

I. INTRODUCTION

Artificial spin ices (ASIs) are lithographically defined nanomagnetic metamaterials in which elongated, single-domain islands are arranged on prescribed lattices, thereby realizing arrays of Ising spins whose moments are locked to their long axes [1]. Geometric design, specifically the lattice spacing, island length/width, and relative orientation, sets the vertex interaction energies and thus controls the array's equilibrium phases and reversal dynamics [2–4]. In many ASI lattices, the geometry of the array and the anisotropy of the dipolar interaction make it impossible to simultaneously minimize all pairwise interactions. This is called geometric frustration, producing a macroscopically degenerate manifold of low-energy states [5]. The geometric frustration and extensive ground-state degeneracy of many ASI lattices make them model platforms for emergent magnetic monopoles [6–11], fast magnetization dynamics [12], phase transitions [13–18], and have inspired ultralow-power spintronic logic and memory devices [19–24].

Among fabricated geometries, the square ASI remains the prototypical and most intensively studied system [1,2,14,17,25]. Four Ising-like nanomagnets meet at each vertex, giving $2^4 = 16$ possible configurations. In the two low-energy "ice-rule" states, type I (T_I) and type II (T_{II}), two moments point in and two point out, yielding zero net magnetic charge. In the standard dumbbell mapping each island is replaced by a pair of opposite magnetic charges $\pm q$ at its ends. Any violation of the 2-in/2-out rule leaves a net charge $Q = \sum_i q_i$ at the vertex and defines an emergent magnetic monopole excitation [9,26]. Reversing a contiguous chain of islands in an otherwise charge-neutral background creates a pair of opposite monopoles. The chain of reversed islands constitutes the Dirac string (DS), and its tension T_{DS} defined as the finite change in energy when the string is extended by one additional spin [see Eq. (2)]; which, together with the magnetic Coulomb interaction between the charges, dictates their dynamics [6,26].

In three-dimensional spin-ice pyrochlores, the DS tension is effectively negligible, so monopoles are deconfined (separating two monopoles arbitrarily far away costs only finite energy [27]), and they interact predominantly via the magnetic Coulomb law [7,26,27]. By contrast, in planar ASIs, nonequivalent distances among four nanomagnets meeting at a vertex, and the anisotropy of dipolar interaction endow the DS with a finite tension, confining opposite charges into bound monopole pairs (BMs); their propagation is largely governed by string tension, rather than by their mutual Coulomb repulsion [6,9,28], although other factors like external fields and disorder can also play a role. Previous studies quantified this confinement and showed that engineering the effective string tension through sub-lattice height offsets [7,9,17], edge engineering [24], or lattice-constant variation [29] can effectively tune the T_{DS} and hence monopole mobility and annihilation pathways. Yet the coupling geometry is frozen once patterned; without the ability to reprogram interisland distances or orientations, achieving reversible sign and magnitude control of T_{DS} (and thus directed "magnetricity" transport) remains difficult.

Kirigami, which cuts and folds a thin sheet into reconfigurable 2D or 3D architectures, offers a mechanically programmable route to overcome this limitation. During

*Contact author: jzcui@fudan.edu.cn

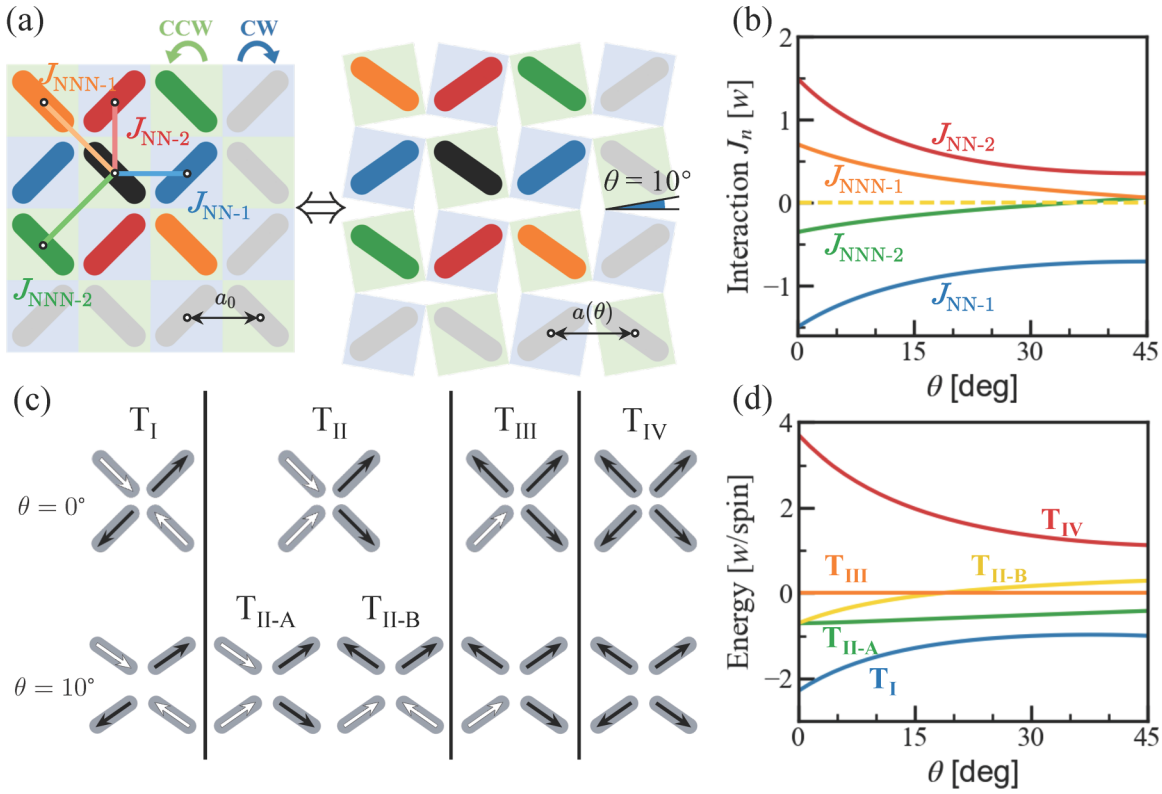

FIG. 1. [(a) and (b)] Kirigami based square ASI with rotation angle $\theta = 0°, 10°$, and the angular dependency of NNI and NNNI. The black spin is taken as the central spin, and the interactions between the central spin and other neighboring spins are shown in (b). Small circles located at the center indicate the location of point-like dipoles. [(c) and (d)] All types of vertices in kirigami based square ASI and the angular dependency of energy of different types of vertices. T_I and T_{II} vertices obey the ice rule, while T_{III} and T_{IV} do not. There are 16 different configurations in total, and only five typical ones shown in (c), and dipoles pointing in are colored white while out are black.

a kirigami transformation, rigid panels pivot about flexible hinges, continuously updating all pairwise distances and relative angles in the embedded lattice and thereby reprogramming dipolar couplings [30,31]. We recently constructed a kirigami-reconfigurable electromagnetic metasurface [32] that substantially extended the accessible wavefront-steering range. In that system, anisotropic meta-atoms are mounted on rigid kirigami panels and co-rotate during the transformation; this rotation tunes their orientation-dependent Pancharatnam-Berry phase and programs the outgoing wavefront. Motivated by that result, we build a model of an ASI on an analogous kirigami scaffold [see Fig. 1(a)], so that mechanical reorientation of the rigid panels reprograms the inter-island dipolar interaction network *in situ*, allowing us to tune the DS tension and thereby reversibly control the monopole motion, including speed and direction. Monte Carlo simulations reveal a DS whose tension crosses through zero as the kirigami rotation angle is varied, enabling controlled reversal of monopole propagation. Because the kirigami scheme relies on a geometric transformation, the same design principle can be implemented with different materials and over a wide range of device sizes. This offers a flexible design framework for reconfigurable "magnetricity" and spintronic devices, although the detailed magnetic response will be governed by the specific material properties and critical dimensions of the fabricated structure [8,24,33,34].

II. MODEL

In this work, we build a model of a square ASI array on a "rotating squares (RS)" kirigami pattern, with each rigid panel carrying one nanomagnet, as shown in Fig. 1(a). During the kirigami transformation, the panels rotate in the plane by an angle θ, alternating clockwise (CW) and counter-clockwise (CCW) on neighboring panels, so the spin lattice naturally divides into two sublattices $\mathbf{S}_{cw}$ and $\mathbf{S}_{ccw}$. We denote by $\mathbf{e}_i(\theta)$ the unit vector along the long (easy) axis of island i after the kirigami rotation. Islands mounted on CW (CCW) panels rotate by $-\theta$ $(+\theta)$ from their zero-angle orientations $\mathbf{e}^0_{CW} = [1,1]/\sqrt{2}$ and $\mathbf{e}^0_{CCW} = [1,-1]/\sqrt{2}$, so $\mathbf{e}_{CW}(\theta) = R(-\theta)\mathbf{e}^0_{CW}$ and $\mathbf{e}_{CCW}(\theta) = R(+\theta)\mathbf{e}^0_{CCW}$, where $R(\theta)$ stands for the rotation matrix in $\mathbb{R}^2$. Each nanomagnet is treated as an Ising variable $\sigma_i = \pm 1$ along its local easy axis, giving $\mathbf{S}_i = \sigma_i \mathbf{e}_i(\theta)$. The center-to-center lattice constant varies with kirigami rotation angle as $a(\theta) = \sqrt{2}a_0 \sin(\theta + \pi/4)$, where a_0 is the lattice constant at $\theta = 0°$. We then model the array with the point dipolar Hamiltonian:

$$\mathcal{H} = w \sum_{i \neq j} \left[\frac{\mathbf{S}_i \cdot \mathbf{S}_j}{r'^3_{ij}} - \frac{3(\mathbf{S}_i \cdot \mathbf{r}'_{ij})(\mathbf{S}_j \cdot \mathbf{r}'_{ij})}{r'^5_{ij}} \right] = - \sum_{i \neq j} J_{ij}(\theta) \sigma_i \sigma_j, \tag{1}$$

where $w = \mu_0 \mu^2 / 4\pi a_0^3$ set the dipolar energy scale at the reference spacing a_0; μ_0 is the permeability of free space, μ is the magnetic moment of an island, and $\mathbf{r}'_{ij} = (\mathbf{r}_i - \mathbf{r}_j)/a_0$

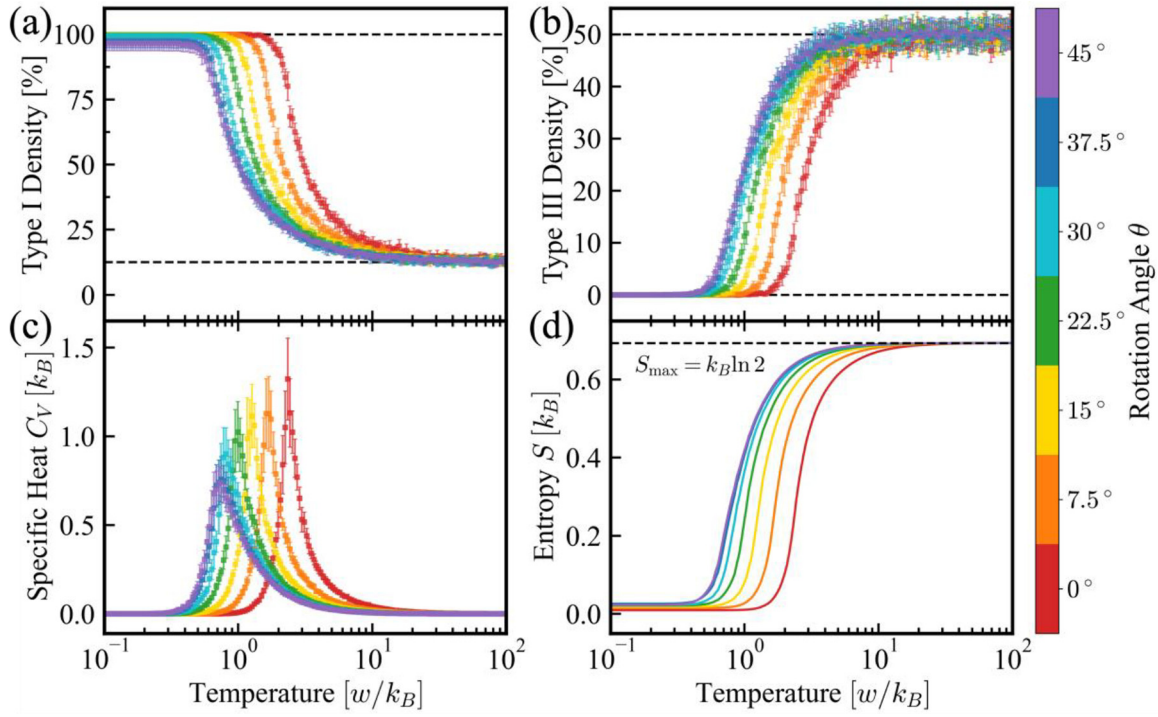

FIG. 2. The T_I vertex density (a) and T_{III} vertex density (b), specific heat (c) and entropy (d), as functions of temperature. Different colors represent systems with different rotation angle θ. (a) The dashed lines indicate the T_I density of a totally random state (12.5%) and a fully ordered state (100%). (b) The dashed lines indicate the T_{III} density of a totally random state (50%) and a low energy state (0%). (c) The specific heat is averaged by twenty parallel simulated annealing, with the error bar representing the standard deviation. (d) Entropy is calculated by integrating the mean specific heat in (c), and at high temperatures, the system is considered paramagnetic, suggesting maximum entropy $S_{\max} = k_B \ln 2$.

is the relative position vector between spin $\mathbf{S}_i$ and $\mathbf{S}_j$. The angle-dependent coupling $J_{ij}(\theta)$ captures both the changing inter-island separations and the rotated easy-axis orientations encoded in $\mathbf{e}_i(\theta)$. Unless noted otherwise, sums run over all spins with open boundary conditions (OBC).

The effective dipolar coupling strengths J between nanomagnets change remarkably with θ, as shown in Fig. 1(b). We label the two nearest-neighbor (NN) interactions as $J_{\mathrm{NN}-1}$ and $J_{\mathrm{NN}-2}$, and the two next-nearest-neighbor (NNN) interactions as $J_{\mathrm{NNN}-1}$ and $J_{\mathrm{NNN}-2}$ [color-coded in Figs. 1(a) and 1(b)]. Because the lattice expands with increasing θ, $J_{\mathrm{NN}-1}$, $J_{\mathrm{NN}-2}$ and $J_{\mathrm{NNN}-1}$ decrease monotonically in magnitude. By contrast, the $J_{\mathrm{NNN}-2}$ coupling undergoes a sign reversal near $\theta \approx 35.3^\circ$, reflecting the changing angle between the spin easy-axis directions and the center-to-center displacement vector $\mathbf{r}'_{ij}$, which toggles the dipolar interaction between ferro- and antiferromagnetic sign [28]. These variations in coupling strength drive pronounced changes in the dipolar energies of the vertices shown in Figs. 1(c) and 1(d). Here we report energy in the unit of the dipolar scale w and do not insert specific magnetic parameters; the corresponding absolute interaction strengths for experimentally relevant island dimensions are discussed later in Sec. V.

Figure 1(d) shows the calculated dipolar energies of the square-ice vertex types as functions of θ. T_I vertices consistently have the lowest energy and T_{IV} the highest. In T_{III} vertices the dominant coupling contributions cancel, yielding a zero energy. Breaking of four-fold symmetry splits the conventional T_{II} class into two distinct subtypes, T_{II-A} and T_{II-B}. At small θ the usual square-ice ordering $T_I < T_{II} < T_{III} < T_{IV}$ persists, which is similar to the Rys-F model with finite energy gap [35], but for $\theta \geqslant 18.5^\circ$ the T_{II-B} branch rises above T_{III}, making a kirigami-driven reordering of the hierarchy of the vertex energy. The θ-dependent reordering of these vertex energies underpins our ability to tune DS tension in the kirigami-reconfigurable ASI.

III. GROUND STATE

Having established the fundamental near-neighbor interactions and the associated vertex energy hierarchy, we proceed to determine the ground state of the new ASI for different rotation angle θ. To this end, we employ the Monte Carlo simulation based on the Metropolis algorithm, implementing a thermal annealing protocol. The thermal annealing protocol starts from a high-temperature $k_BT = 100w$. Each temperature update is set to 96% of the previous temperature value until the temperature $k_BT < 0.1w$, and each temperature update includes 2,000 Monte Carlo steps (MCS).

Figures 2(a) and 2(b) illustrate the evolution of T_I and T_{III} vertex densities throughout the annealing process. As the system cools, T_I vertices become predominant, while T_{III} vertices become increasingly scarce. Upon completion of the thermal annealing protocol, the final state consists almost exclusively of T_I vertices, independent of the rotation angle of the system.

The energy of ASI during annealing is used to compute the specific heat per spin, shown in Fig. 2(c). Integration of the specific heat curves yields the entropy per spin, presented in Fig. 2(d) (see Sec. S1 of Ref. [36] (including Refs. [35,37]) for details of calculation and comparison with Rys-F model). At low temperatures, the entropy approaches zero, suggesting that the ASI anneals into a long-range ordered ground state composed solely of T_I vertices. This paramagnetic-antiferromagnetic phase transition is further corroborated by the peaks observed in the specific heat curves in Fig. 2(c). For systems with larger θ, the residual entropy is slightly higher, indicating that a longer annealing time and a slower cooling rate may be required to reach the fully ordered T_I ground state. This behavior points to distinct dynamic characteristics depending on the rotation angle.

IV. ENERGETICS OF DIRAC STRINGS

The fact that the angle-dependent dipolar couplings established in Fig. 1(b) change the hierarchy of vertex energy in Fig. 1(d) suggests that both BM motion dynamics and DS energetics should be tunable by the kirigami rotation angle θ. We therefore construct DSs numerically in a 200×200-spin array by flipping a contiguous row of spins in an ordered background. In square ice, a DS consists of 2-in/2-out vertices whose type differs from the background, while the two ends host 3-in/1-out and 1-in/3-out (T_{III} vertices) monopoles. Because the three distinct lowest-energy backgrounds (T_I, T_{II-A}, and T_{II-B}) can pair $3 \times 2 = 6$ ordered ways, the system admits six elementary DSs denoted "T_X DS in T_Y" (T_X for the vertices along the string, T_Y for the background). Earlier work [6] had examined only the symmetric pair T_I DS in T_{II} and T_{II} DS in T_I; based on the kirigami lattice, we reveal the previously overlooked combinations T_{II-A} DS in T_{II-B} and T_{II-B} DS in T_{II-A}. Spin configurations and per-spin energy maps for the three representative DSs at $\theta = 0^\circ$ are shown in Figs. 3(a)–3(c). Full profiles for all six strings are given in Sec. S2 of Ref. [36].

To quantify string energetics, we refer to Ref. [6] and compute the difference between $E_{DS}(r)$, the energy of ASI with a string of length r and E_0, the energy of background (see Secs. S3 and S4 of Ref. [36]). This difference, i.e., $U(r) = E_{DS}(r) - E_0$, demonstrating the energy change for producing a DS. If $U(r) > 0$, producing the DS lifts the total energy of ASI and vice versa. According to Ref. [6], $U(r)$ can be fitted by the standard form:

$$U(r) = T_{DS} r - \Psi(r) \approx T_{DS} r - \gamma / r + \text{const.}, \qquad (2)$$

where γ represents the strength of Coulomb repulsion between the BM pair, and T_{DS} is the string tension in the unit of w/spin. According to simple mathematics (see Sec. S2 of Ref. [36]), T_{DS} is governed by the single-spin energy difference between the string and its background, $\Delta e = e_{DS} - e_0$ [see double arrows in Fig. 3(d)]; quantitatively, we have $T_{DS} = 2\Delta e$. Spatial energy profiles for strings of length $r = 50$ [spin] at $\theta = 0^\circ$ are plotted in Figs. 3(d)–3(f), illustrating this energy difference Δe and hence the origin of T_{DS}. A small rotation to $\theta = 5^\circ$ is enough to differentiate the three examples: for the T_{II-A} DS the T_I background energy drops while the string energy is almost unchanged, enlarging their gap; the T_I DS remains below the T_{II-B} background and the gap widens slightly as both energies drop; most strikingly, the T_{II-B} DS in T_{II-A} background crosses from higher to lower energy, switching the sign of Δe, i.e., the sign of T_{DS} as well.

Figure 3(g) compiles the tension T_{DS} of every string against the kirigami angle and reveals three distinct behaviors. First, strings embedded in a T_I background (i.e., T_{II-A} DS in T_I and T_{II-B} DS in T_I) show a monotonic decrease in $|T_{DS}|$ as θ grows, a direct consequence of the uniform lattice dilation. A comparable attenuation is found for the two configurations whose DS is T_I but whose background is T_{II-A} or T_{II-B}. By contrast, the two strings formed within T_{II} background evolve in opposite directions: the T_{II-A} DS in T_{II-B} shows a steadily increasing tension as the rotation angle grows, while the T_{II-B} DS in T_{II-A} loses tension, crosses $T_{DS} = 0$ near $\theta \approx 1^\circ$, and subsequently becomes positive, producing a mechanically induced reversal of the tension on its BM pair. This sign switch mainly results from two distinct mechanisms: the large enough next-nearest neighboring interactions J_{NNN-2} cause the initial negative sign, while the geometric asymmetry from the kirigami transformation causes the subsequent positive sign with the increase of θ (see analysis in Sec. S5 of Ref. [36]). The fitted values of tension derived from a finite system [see symbols in Fig. 3(g)] match the analytic results derived from a system with infinite spins [see dashed curves in Fig. 3(g)]. (Derivations and explicit forms of these analytic results can be found in Sec. S3–S6 of Ref. [36].) Kirigami rotation, therefore, provides a reversible, purely geometric means to program DS tension and steer monopole currents in ASI.

To assess the robustness of the sign switch phenomenon and its potential dependence on the point-dipole approximation, we have implemented a dumbbell model that incorporates a finite charge separation ℓ. This analysis confirms that the kirigami-based control of monopole dynamics remains operative across a broad range of ℓ, thereby corroborating the generality of our conclusions.

According to Ref. [38], in the dumbbell representation, each island is modeled as a pair of opposite magnetic charges $q = \pm\mu/\ell$ separated by a distance ℓ along the long axis of the island, and μ is the magnetic moment. The parameter $0 < \ell < \sqrt{2}a_0$ controls the ratio of the wire length to the vertex separation: $\ell \to 0$ reproduces the point-dipole limit, where $\ell \to \sqrt{2}a_0$ corresponds to a continuously connected ASI where the dumbbell description ceases to be meaningful. The Hamiltonian of the dumbbell model is then shown as follows:

$$\mathcal{H} = \frac{\mu_0}{4\pi} \sum_{i \neq j} \frac{q_i q_j}{r_{ij}}, \qquad (3)$$

where r_{ij} represents the distance between the charges q_i and q_j. Interactions between the two charges belonging to the same island only contribute a constant self-energy and are therefore ignored, since spin flips do not change this contribution. Open boundary conditions are applied in the calculation for consistency. For a direct comparison with the point-dipole model, the calculated energies are expressed in the unit of $w = \mu_0 \mu^2 / 4\pi a_0^3$.

We compute the total energy $U(r)$ of T_{II-B} DSs in T_{II-A} background using both the point-dipole and dumbbell models;

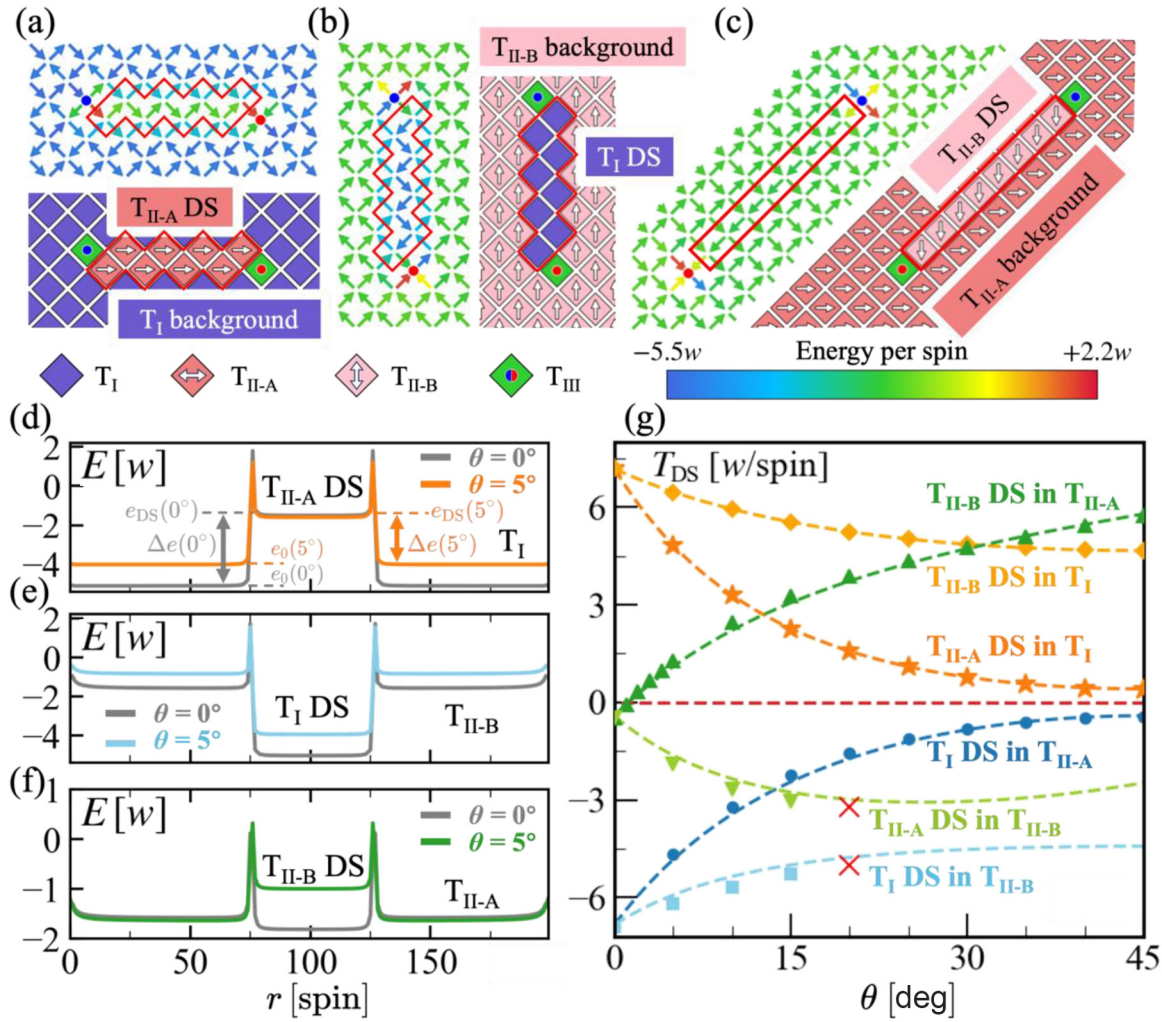

FIG. 3. [(a)–(c)] The microscopic configurations of three typical DSs in kirigami based square ASI for static calculations. The color of the arrows gives the energy per spin, while the rhombuses correspond to the vertices. [(d)–(f)] Spatial energy profile along the DSs of (a)–(c), and the influence of θ. (g) The angular dependency of tensions of all kinds of DSs. The dots show the results of static calculation in a 200×200 spins system by OBC, and the dashed lines show the semi-analytical results for a system with infinite spins. The red cross indicates the instability of T_{II-B} background from which many monopoles spontaneously emerge. For $\theta \geqslant 18.5°$, the T_{II-B} background becomes so unstable that a large number of monopoles emerge even at very low temperature, leading to the spontaneous breakdown of the ordered T_{II-B} background and making it impossible to study the DS behavior in a T_{II-B} ordered background.

where the results are presented in Fig. 4. In Fig. 4(a), we fix the rotation angle $\theta = 0°$, and vary the model parameter ℓ from $\ell = 0$ (point-dipole model) to $\ell = 1.2a_0$, with different colors representing distinct ℓ values. For all ℓ, $U(r)$ exhibits a decreasing trend when $r \geqslant 5$, implying a negative tension via Eq. (2). Moreover, although $U(r) > 0$ indicating that nucleating a T_{II-B} DS in T_{II-A} background is energetically unfavorable, once its length exceeds $r \geqslant 5$, the string can extend spontaneously because $dU/dr < 0$. Figure 4(b) shows $U(r)$ for $\theta = 5°$. Here the clear increasing trend indicates a positive tension. A comparison of Figs. 4(a) and 4(b) demonstrates that the sign switch of the tension occurs consistently across a broad range of the parameter ℓ. Fitting Eq. (2) to the data in Figs. 4(a) and 4(b) yields the tension T_{DS} and the Coulomb repulsion factor γ, plotted in Figs. 4(c) and 4(d), respectively. Figure 4(c) reveals that while ℓ can substantially affect the magnitude of T_{DS}, its sign remains unchanged for fixed θ; increasing θ drives the sign switch. From Fig. 4(d), we observe that γ is nearly independent of ℓ and decreases with θ. In summary, the sign switch of the string tension identified in Fig. 3(g) is not peculiar to the point-dipole approximation but persists in the dumbbell model over a wide interval of the parameter ℓ. Energy profiles of DSs using dumbbell models can be found in Sec. S7 of Ref. [36] (including Refs. [6,24,28,38]).

V. DYNAMIC PROPERTIES OF T_{II-B} DIRAC STRINGS IN T_{II-A}

To test how reliably the sign of T_{DS} predicts the dynamic behavior of BMs, we focus on the T_{II-B} DS in a T_{II-A} background whose tension changes sign near $\theta = 1°$. Figures 5(a)–5(c) and 5(d)–5(f) show snapshots of the Monte Carlo annealing process of this string at $\theta = 0°$ and $\theta = 5°$, respectively, without an external field. At $\theta = 0°$, the tension is negative and the string is expected to grow; indeed, the

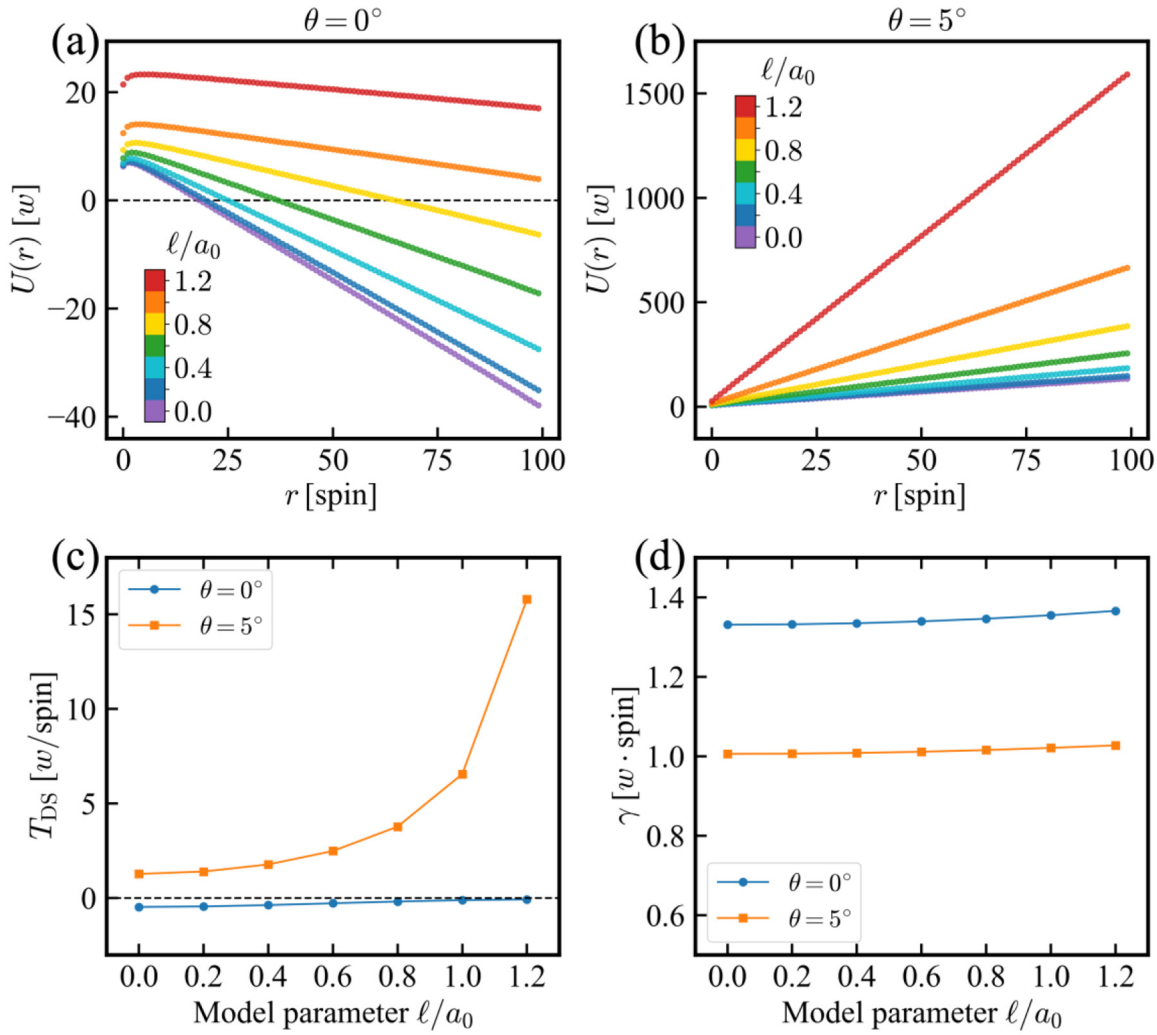

FIG. 4. Model dependence of the energetics of T_{II-B} DS in T_{II-A} background. [(a) and (b)] Total energy $U(r)$ for different rotation angle $\theta = 0^\circ$ (a) and $\theta = 5^\circ$ (b); different colors are used to show different model parameter ℓ/a_0 we use, from 0 (purple) to 1.2 (red). [(c) and (d)] The DS tension T_{DS} (c) and the strength of Coulomb repulsion γ (d) derived from fitting Eq. (2) to the data in (a) and (b).

T_{II-B} segment (pink bar) spontaneously elongates along the diagonal. At $\theta = 5^\circ$, the tension is already positive and should drive shrinkage, yet the simulation still shows net expansion. The energy maps reveal that, in both cases, growth is accompanied by copious nucleation of T_I vertices (blue diamonds), suggesting that local monopole dynamics can override the tendency set by the string tension.

To quantify the local dynamics [39] of monopoles, we evaluate the single-spin flipping probability using the Metropolis algorithm

$$P(\mathbf{S}_i) = \frac{1}{Z} \min\left\{1, \exp\left(-\frac{\Delta E_i}{k_B T}\right)\right\}, \tag{4}$$

where $Z = \sum_i \min\{1,\ \exp(-\Delta E_i/(k_B T))\}$ is the partition function; summation is calculated over the four spins consisting of the specific monopole; ΔE_i is the energy difference of flipping spin $\mathbf{S}_i$. Figure 5(m) plots P versus θ for those four spins at the positive monopole of the T_{II-B} string (color code matches the spins sketched in the inset). Red and blue flips, respectively, lengthen and shorten the T_{II-B} string, whereas green flips create T_I vertices that also lengthen it. As θ increases, the red-versus-blue imbalance weakens, consistent with the rising positive tension, but the probability of the green flip remains high (see Sec. S8 of Ref. [36]), so the T_I-vertex channel still drives expansion. In other words, the string tension only characterizes the energy cost of propagation along the string, whereas additional pathways mediated by T_I-vertex nucleation might dominate the overall monopole dynamics. Nonetheless, this "off-rail" pathway can be suppressed by a modest in-plane field. Applying $\mu_0 \mathbf{H}_{ext} = 2.5w$ at 45 ° to the lattice [see arrow in Fig. 5(n)] raises the energy barrier for the green flip resulting flipping probability close to zero, as shown in Fig. 5(n). The corresponding snapshots, Figs. 5(g)–5(i) at $\theta = 0^\circ$ and Figs. 5(j)–5(l) at $\theta = 5^\circ$, show that the DS now grows at negative tension and shrinks once $T_{DS} > 0$. A complete movie of all six DSs under zero and finite field is provided in Movies SI2 and SI3 (description of movies and simulation details shown in Secs. S9 and S10 of Ref. [36]).

In the figures and movies discussed above, time is quantified in Monte Carlo steps and does not yet correspond

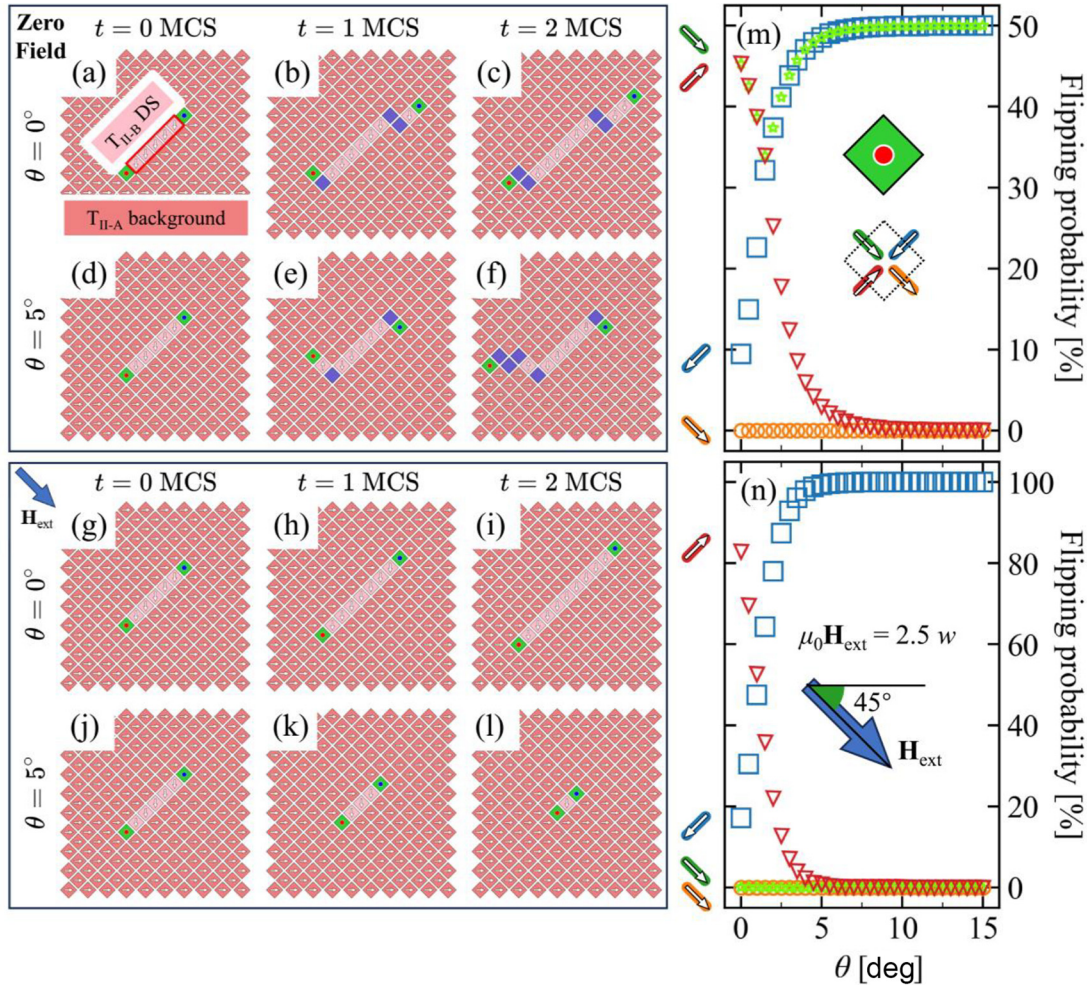

FIG. 5. [(a)–(f)] Snapshots of evolvement of T_{II-B} DS in T_{II-A} without an external magnetic field: (a)–(c) kirigami based square ASI with $\theta = 0^\circ$ and (d)–(f) for $\theta = 5^\circ$. [(g)–(l)] Snapshots of evolvement of T_{II-B} DS in T_{II-A} with external magnetic field H_{ext}: (g)–(i) kirigami based square ASI with $\theta = 0^\circ$ and (j)–(l) for $\theta = 5^\circ$. [(m) and (n)] Angular dependency of flipping probabilities of four spins consisting of the north pole monopole (red one) at $t = 0$. Color of markers corresponds to the color of spins for insets in (m). Inset in (n) gives the magnitude and direction of H_{ext}.

to a specific physical timescale. By incorporating realistic magnetic parameters and introducing switching barriers for individual spins, we can estimate the physical timescale and demonstrate that the evolution of DS should be observable within experimentally feasible time frames. According to Ref. [24], the dynamics of the thermally assisted, spontaneous wire switch can be described by a transition rate $\nu(E_T, T)$ of the form

$$\nu(E_T, T) = \nu_0 \exp\left(-\frac{E_T}{k_B T}\right), \tag{5}$$

where ν_0 is the attempt frequency, k_B is the Boltzmann constant, and T is the temperature. The barrier energy $E_T = E_b + (1/2)E_{m\to l}$ represents the total energy required for a single wire to switch, comprising the intrinsic switching barrier energy E_b and the change in dipolar energy $E_{m\to l}$ associated with the transition from the initial to the final magnetic configuration. For the switching of a specific spin $\mathbf{S}_i$, the difference in dipolar energy $E_{m\to l}$ corresponds exactly to ΔE_i as defined in Eq. (4). Adopting the parameters in Ref. [24], we consider a permalloy ($Fe_{80}Ni_{20}$) magnetic island with dimensions $470 \times 170 \times 3\,\text{nm}$ and a nearest-neighbor distance $a_0 = 424\,\text{nm}$. The coupling factor is given by $w = \mu_0\mu^2/4\pi a_0^3 = 9.22 \times 10^{-21}\,[\text{J}] = 0.06\,[\text{eV}] \sim 667\,[\text{K}]$. The attempt frequency is $\nu_0 = 10^9\,[\text{s}^{-1}]$, and the switching barrier for a magnetic island $E_b = 0.626\,[\text{eV}] \approx 10.88w$. Using these data, we estimate that, at a relatively low temperature, e.g., $T = 0.5\ [w/k_B] \approx 334\,[\text{K}]$, the average time required for a T_{II-B} DS in T_{II-A} (for $\theta = 0^\circ$) to extend by one spin is approximately 16.6 [s]. This timescale is well within a practically observable range, making the DS evolvement accessible to techniques such as x-ray magnetic circular dichroism [9]. Further technical details regarding the calculation and an analysis of geometric disorder are provided in Secs. S11 and S12 of Ref. [36] (including Refs. [9,11,40,41]).

In summary, these results emphasize that the scalar tension governs the force on a Dirac string along a specific direction, but the actual motion of bound monopoles also depends on local dynamics, namely the flipping probabilities of spins at the monopole. External fields, or other symmetry-breaking perturbations, therefore offer a practical route to align microscopic spin kinetics with the mechanically

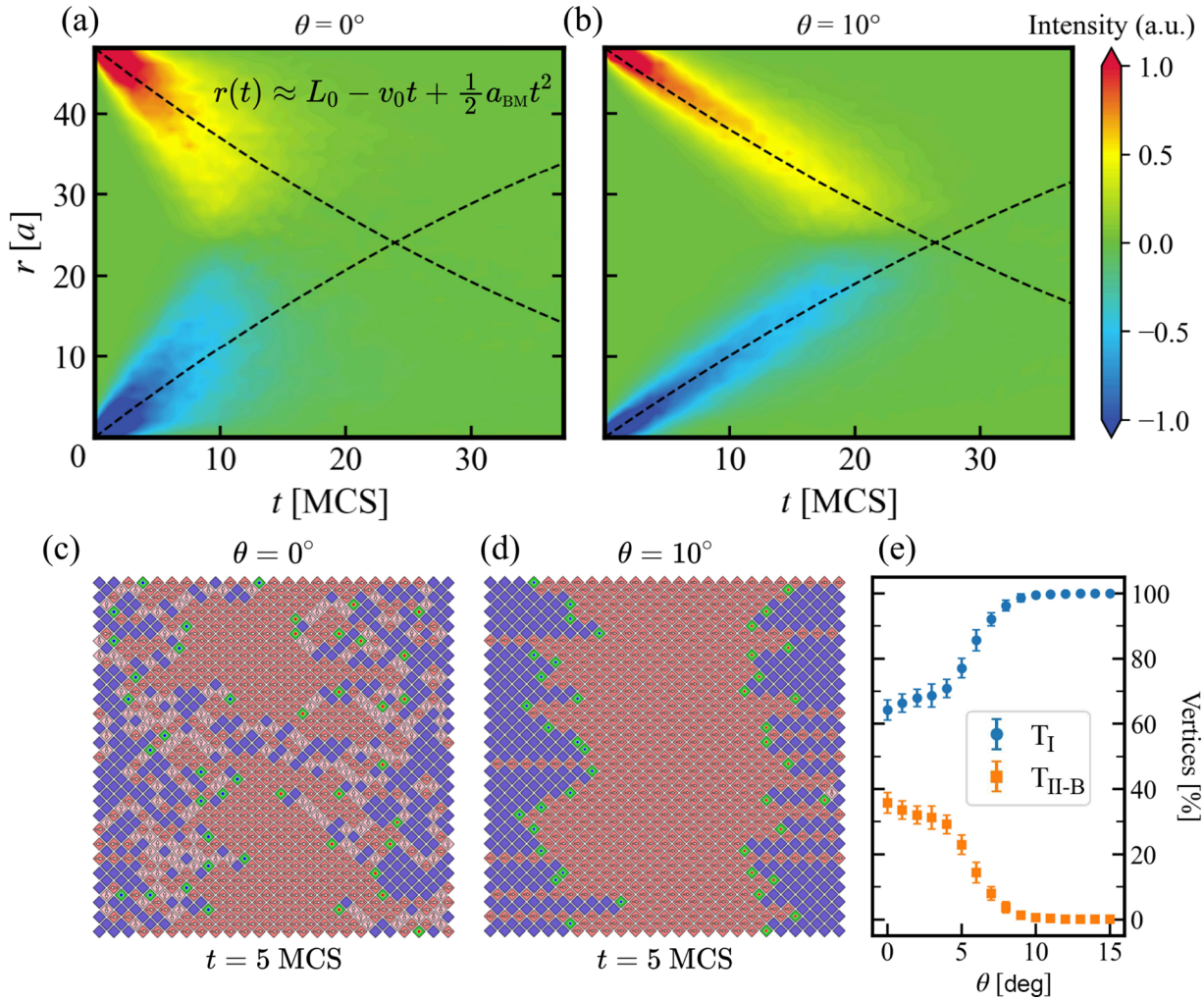

FIG. 6. [(a) and (b)] Monte Carlo path-time diagrams of multiple DSs at $k_BT = 0.2w$ for $\theta = 0^\circ$ (a) and $\theta = 10^\circ$ (b), averaged by 100 independent simulations. The color scheme gives the mean strength of BMs at the ends of DSs. Initial DS length is $L = 50$ [spin]. Dashed lines show the fitted Eq. (6). In (a) and (b), the acceleration is $a_{\mathrm{BM}} \approx 7.2 \times 10^{-3}$ [spin/MCS^2] and 5.9×10^{-3} [spin/MCS^2], respectively. (c) and (d) show snapshots of the path-time diagrams in (a) and (b) at $t = 5$ MCS. (e) gives the average proportions of vertices generated by the motion of BMs at $t = 5$ MCS, the error bars show the standard deviation.

programmed tensions, and thereby with the desired BM motions, in kirigami-reconfigurable artificial spin ice.

VI. COLLECTIVE DYNAMICS OF BOUND MONOPOLES

To explore collective BM motion effects, we turned to $\mathrm{T_{II-A}}$ string in a $\mathrm{T_I}$ background, the configuration whose tension decreases most strongly with kirigami rotation [see Fig. 3(g)]. Figures 6(a) and 6(b) track the average monopole trajectories for 100 strings of initial length $L_0 = 50$ [spin] at $\theta = 0^\circ$ and $\theta = 10^\circ$, respectively. The color scale represents the instantaneous BM density; dashed lines are fits to the analytical result derived from [6]

$$r(t) \approx L_0 - 2t\sqrt{\frac{L_0 T_{\mathrm{DS}}}{2m}} + t^2\frac{T_{\mathrm{DS}}}{2m}, \tag{6}$$

where $m \approx 500$ $[w/c^2]$ is the monopole mass [6] (c is the light speed), and T_{DS} is taken from Fig. 3(g). The smaller tension at $\theta = 10^\circ$ ($T_{\mathrm{DS}} \approx 3.3$ $[w/\mathrm{spin}]$) lowers the fitted value of acceleration from 7.2×10^{-3} to 5.9×10^{-3} [spin/MCS^2], confirming that kirigami rotation slows the mean BM speed in quantitative accord with Eq. (6). Kirigami deformation also sharpens the directionality of the motion: the path map at $\theta = 0^\circ$ is diffuse, whereas the $\theta = 10^\circ$ map collapses into a narrow horizontal band, indicating highly linear, almost purely horizontal motion. Figs. 6(c) and 6(d) show the snapshots of evolvement at $t = 5$ MCS (see the complete evolvement and time-dependent vertex density analysis in Movie SI4 and Sec. S13 of Ref. [36]). Vertex statistics in Fig. 6(e) clarify this transition: at $\theta = 0^\circ$ the newly generated vertices are a roughly even mix of $\mathrm{T_I}$ vertices, which straighten the string, and $\mathrm{T_{II-B}}$ vertices, which make it meander, whereas at $\theta = 10^\circ$ almost every new vertex is $\mathrm{T_I}$ and $\mathrm{T_{II-B}}$ creation is nearly suppressed, yielding an almost perfectly straight string. This reflects the rotation-driven bias in single-spin flipping probabilities (see Sec. S8 of Ref. [36]), and this probability bias underlies both the enhanced linearity

of DSs and the dramatically shorter percolation times discussed in Sec. S14 of Ref. [36] (including reference [42]). Thus, the kirigami scaffold provides simultaneous control over BM speed through tension and BM directionality through modified local dynamics.

VII. CONCLUSIONS AND DISCUSSIONS

The RS kirigami scaffold demonstrates that purely geometric actuation can program both the energy landscape and the experimentally relevant time scale of monopole propagation in artificial spin ice. By varying a single mechanical parameter—the in-plane rotation angle—we continuously tuned the DS tension, reversed the direction of BM motion, and modulated collective speed and directionality. Because the scheme relies only on planar cuts and hinges, it can be implemented to ASIs within submicrometer regime by standard CMOS-compatible nanofabrication [43–45]. The approach is intrinsically material- and scale-independent, offering a versatile route to reconfigurable "magnetricity" elements and other spin-based devices. Beyond providing a quantitative picture of how monopole interactions are reshaped by lattice reconfiguration, our results highlight two complementary control knobs: global geometry, which sets the string tension and local spin-flip dynamics of monopoles, which largely govern the monopole propagation throughout the lattice. Combining kirigami actuation with time-dependent magnetic, electric, or strain fields, or embedding more intricate kirigami patterns, should enable even finer control over monopole creation, transport, and annihilation, opening new opportunities for low-power spintronic logic, memory, and neuromorphic architectures based on topological defects.

ACKNOWLEDGMENTS

This work is supported by the National Key Technologies R&D Program of China Grants No. (2022YFA1404700 and No. 2022YFA1207000), National Natural Science Foundation of China Grant No. (62375054), Shanghai Rising-Star Program Grant No. (24QA2700700), Science and Technology Commission of Shanghai Municipality (Grants No. 24520750200, No. 24CL2900200, and No. 25JD1404500), and Shanghai Talent Programs. The computations in this research were performed using the Computing for the Future at Fudan (CFFF) platform of Fudan University.

DATA AVAILABILITY

The data that support the findings of this article are openly available [46].

[1] R. F. Wang, C. Nisoli, R. S. Freitas, J. Li, W. McConville, B. J. Cooley, M. S. Lund, N. Samarth, C. Leighton, V. H. Crespi, *et al.*, Artificial 'spin ice' in a geometrically frustrated lattice of nanoscale ferromagnetic islands, Nature (London) **439**, 303 (2006).

[2] S. H. Skjærvø, C. H. Marrows, R. L. Stamps, and L. J. Heyderman, Advances in artificial spin ice, Nat. Rev. Phys. **2**, 13 (2019).

[3] C. Nisoli, R. Moessner, and P. Schiffer, *Colloquium*: Artificial spin ice: Designing and imaging magnetic frustration, Rev. Mod. Phys. **85**, 1473 (2013).

[4] A. Ortiz-Ambriz, C. Nisoli, C. Reichhardt, C. J. O. Reichhardt, and P. Tierno, *Colloquium*: Ice rule and emergent frustration in particle ice and beyond, Rev. Mod. Phys. **91**, 041003 (2019).

[5] I. Gilbert, C. Nisoli, and P. Schiffer, Frustration by design, Phys. Today(7) **69**, 54 (2016).

[6] E. Y. Vedmedenko, Dynamics of bound monopoles in artificial spin ice: How to store energy in dirac strings, Phys. Rev. Lett. **116**, 077202 (2016).

[7] L. A. S. Mól, W. A. Moura-Melo, and A. R. Pereira, Conditions for free magnetic monopoles in nanoscale square arrays of dipolar spin ice, Phys. Rev. B **82**, 054434 (2010).

[8] H. Arava, E. Y. Vedmedenko, J. Cui, J. Vijayakumar, A. Kleibert, and L. J. Heyderman, Control of emergent magnetic monopole currents in artificial spin ice, Phys. Rev. B **102**, 144413 (2020).

[9] A. Farhan, M. Saccone, C. F. Petersen, S. Dhuey, R. V. Chopdekar, Y.-L. Huang, N. Kent, Z. Chen, M. J. Alava, T. Lippert, *et al.*, Emergent magnetic monopole dynamics in macroscopically degenerate artificial spin ice, Sci. Adv. **5**, eaav6380 (2019).

[10] S. Ladak, D. E. Read, G. K. Perkins, L. F. Cohen, and W. R. Branford, Direct observation of magnetic monopole defects in an artificial spin-ice system, Nat. Phys. **6**, 359 (2010).

[11] E. Mengotti, L. J. Heyderman, A. F. Rodríguez, F. Nolting, R. V. Hügli, and H.-B. Braun, Real-space observation of emergent magnetic monopoles and associated Dirac strings in artificial kagome spin ice, Nat. Phys. **7**, 68 (2011).

[12] S. Gliga, A. Kákay, R. Hertel, and O. G. Heinonen, Spectral analysis of topological defects in an artificial spin-ice lattice, Phys. Rev. Lett. **110**, 117205 (2013).

[13] W.-C. Yue, Z. Yuan, Y.-Y. Lyu, S. Dong, J. Zhou, Z.-L. Xiao, L. He, X. Tu, Y. Dong, H. Wang, *et al.*, Crystallizing kagome artificial spin ice, Phys. Rev. Lett. **129**, 057202 (2022).

[14] D. Levis, L. F. Cugliandolo, L. Foini, and M. Tarzia, Thermal phase transitions in artificial spin ice, Phys. Rev. Lett. **110**, 207206 (2013).

[15] J. Sklenar, Y. Lao, A. Albrecht, J. D. Watts, C. Nisoli, G.-W. Chern, and P. Schiffer, Field-induced phase coexistence in an artificial spin ice, Nat. Phys. **15**, 191 (2019).

[16] L. Anghinolfi, H. Luetkens, J. Perron, M. G. Flokstra, O. Sendetskyi, A. Suter, T. Prokscha, P. M. Derlet, S. L. Lee, and L. J. Heyderman, Thermodynamic phase transitions in a frustrated magnetic metamaterial, Nat. Commun. **6**, 8278 (2015).

[17] Y. Perrin, B. Canals, and N. Rougemaille, Extensive degeneracy, Coulomb phase and magnetic monopoles in artificial square ice, Nature (London) **540**, 410 (2016).

[18] Y. Xie, P. Li, S. Zheng, M. Liu, and J.-M. Liu, An improved artificial spin ice structure for restoring ice degeneracy, J. Appl. Phys. **136**, 034304 (2024).

[19] M. T. Kaffash, S. Lendinez, and M. B. Jungfleisch, Nanomagnonics with artificial spin ice, Phys. Lett. A **402**, 127364 (2021).

[20] J. H. Jensen, E. Folven, and G. Tufte, Computation in artificial spin ice, in *The 2018 Conference on Artificial Life* (MIT Press, Tokyo, Japan, 2018), pp. 15–22.

[21] H. Li, L. Li, R. Xiang, W. Liu, C. Yan, Z. Tao, L. Zhang, and R. Liu, Physical reservoir computing and deep neural networks using artificial and natural noncollinear spin textures, Phys. Rev. Appl. **22**, 014027 (2024).

[22] W. Hu, Z. Zhang, Y. Liao, Q. Li, Y. Shi, H. Zhang, X. Zhang, C. Niu, Y. Wu, W. Yu, *et al.*, Distinguishing artificial spin ice states using magnetoresistance effect for neuromorphic computing, Nat. Commun. **14**, 2562 (2023).

[23] J. C. Gartside, K. D. Stenning, A. Vanstone, H. H. Holder, D. M. Arroo, T. Dion, F. Caravelli, H. Kurebayashi, and W. R. Branford, Reconfigurable training and reservoir computing in an artificial spin-vortex ice via spin-wave fingerprinting, Nat. Nanotechnol. **17**, 460 (2022).

[24] H. Arava, N. Leo, D. Schildknecht, J. Cui, J. Vijayakumar, P. M. Derlet, A. Kleibert, and L. J. Heyderman, Engineering relaxation pathways in building blocks of artificial spin ice for computation, Phys. Rev. Appl. **11**, 054086 (2019).

[25] G. Möller and R. Moessner, Artificial square ice and related dipolar nanoarrays, Phys. Rev. Lett. **96**, 237202 (2006).

[26] L. A. Mól, R. L. Silva, R. C. Silva, A. R. Pereira, W. A. Moura-Melo, and B. V. Costa, Magnetic monopole and string excitations in two-dimensional spin ice, J. Appl. Phys. **106**, 063913 (2009).

[27] R. Moessner, Spin ice as a Coulomb liquid: From emergent gauge fields to magnetic monopoles, in *Spin Ice*, edited by M. Udagawa, and L. Jaubert (Springer International Publishing, Cham, 2021), Vol. 197, pp. 37–70.

[28] D. Louis, D. Lacour, M. Hehn, V. Lomakin, T. Hauet, and F. Montaigne, A tunable magnetic metamaterial based on the dipolar four-state Potts model, Nat. Mater. **17**, 1076 (2018).

[29] D. G. Duarte, L. B. De Oliveira, F. S. Nascimento, W. A. Moura-Melo, A. R. Pereira, and C. I. L. De Araujo, Magnetic monopole free motion in two-dimensional artificial spin ice, Appl. Phys. Lett. **124**, 112413 (2024).

[30] G. P. T. Choi, L. H. Dudte, and L. Mahadevan, Programming shape using kirigami tessellations, Nat. Mater. **18**, 999 (2019).

[31] L. Jin, A. E. Forte, B. Deng, A. Rafsanjani, and K. Bertoldi, Kirigami-inspired inflatables with programmable shapes, Adv. Mater. **32**, 2001863 (2020).

[32] G. Jiang, Y. Wang, Z. Zhang, W. Pan, Y. Chen, Y. Wang, X. Chen, E. Song, G. Huang, Q. He, *et al.*, Abnormal beam steering with kirigami reconfigurable metasurfaces, Nat. Commun. **16**, 1660 (2025).

[33] J. Loehr, A. Ortiz-Ambriz, and P. Tierno, Defect dynamics in artificial colloidal ice: Real-time observation, manipulation, and logic gate, Phys. Rev. Lett. **117**, 168001 (2016).

[34] Y.-L. Wang, X. Ma, J. Xu, Z.-L. Xiao, A. Snezhko, R. Divan, L. E. Ocola, J. E. Pearson, B. Janko, and W.-K. Kwok, Switchable geometric frustration in an artificial-spin-ice–superconductor heterosystem, Nat. Nanotechnol. **13**, 560 (2018).

[35] C. Nisoli, Topological order of the Rys F-model and its breakdown in realistic square spin ice: Topological sectors of Faraday loops, Europhys. Lett. **132**, 47005 (2020).

[36] See Supplemental Material at http://link.aps.org/supplemental/10.1103/q1vr-p9v4 for description of analytical calculations and relative videos.

[37] H. Saglam, A. Duzgun, A. Kargioti, N. Harle, X. Zhang, N. S. Bingham, Y. Lao, I. Gilbert, J. Sklenar, J. D. Watts, *et al.*, Entropy-driven order in an array of nanomagnets, Nat. Phys. **18**, 706 (2022).

[38] F. S. Nascimento, L. B. De Oliveira, D. G. Duarte, C. I. L. De Araujo, W. A. Moura-Melo, and A. R. Pereira, Conditions for an emergent gauge field in planar artificial spin ices with the dumbbell model approach, J. Appl. Phys. **135**, 244307 (2024).

[39] V. Schánilec, O. Brunn, M. Horáček, S. Krátký, P. Meluzín, T. Šikola, B. Canals, and N. Rougemaille, Approaching the topological low-energy physics of the F model in a two-dimensional magnetic lattice, Phys. Rev. Lett. **129**, 027202 (2022).

[40] M. Menniti, N. Leo, P. Villalba-González, M. Pancaldi, and P. Vavassori, Relaxation pathways and emergence of domains in square artificial spin ice, Phys. Rev. B **112**, 134410 (2025).

[41] R. B. Schinazi, Continuous-time birth and death chains, in *Classical and Spatial Stochastic Processes* (Springer Nature Switzerland, Cham, 2024), pp. 179–199.

[42] P. Reynolds, H. Stanley, and W. Klein, Large-cell Monte Carlo renormalization group for percolation, Phys. Rev. B **21**, 1223 (1980).

[43] Z. Liu, H. Du, J. Li, L. Lu, Z.-Y. Li, and N. X. Fang, Nano-kirigami with giant optical chirality, Sci. Adv. **4**, eaat4436 (2018).

[44] X. Hong, B. Xu, G. Li, F. Nan, X. Wang, Q. Liang, W. Dong, W. Dong, H. Sun, Y. Zhang, *et al.*, Optoelectronically navigated nano-kirigami microrotors, Sci. Adv. **10**, eadn7582 (2024).

[45] S. Chen, Z. Liu, H. Du, C. Tang, C.-Y. Ji, B. Quan, R. Pan, L. Yang, X. Li, C. Gu, *et al.*, Electromechanically reconfigurable optical nano-kirigami, Nat. Commun. **12**, 1299 (2021).

[46] https://doi.org/10.5281/zenodo.18932357.